



Fabrication of Nanocellulose/Chitosan Nanocomposite Based on Loofah Sponge for Efficient Removal of Methylene Blue: Thermodynamic and Kinetic Investigations

E. A. Matter¹ · Asaad F. Hassan¹ · Nourhan M. Elfaramawy¹ · Ghada Esmail¹

Received: 16 April 2024 / Accepted: 15 May 2024
© The Author(s) 2024

Abstract

We established three nano-solid adsorbents: nanocellulose based on plant loofah sponge (NC), chitosan (CS), and nanocellulose/chitosan composite (CSC). These substances were employed as solid adsorbents to eliminate methylene blue (MB) dye from wastewater. Various characterization techniques were employed to investigate all the synthesized solid adsorbents, including TGA (thermogravimetric analysis), XRD (X-ray diffraction spectra), (BET) nitrogen gas adsorption-desorption, SEM (scanning electron microscope), TEM (transmission electron microscopy), FTIR (Fourier transform infrared) spectrometer, and zeta potential. According to our results, CSC showed greater thermal stability than LS and NC but lower than CS, mesoporous (2.012 nm), higher total pore volume ($0.366 \text{ cm}^3 \cdot \text{g}^{-1}$), specific surface area ($639.3 \text{ m}^2 \cdot \text{g}^{-1}$), and pH_{pzc} of 7.22. The static adsorption of MB was well described by the Langmuir ($R^2 > 0.9872$), Temkin ($R^2 > 0.9668$), and Dubinin-Radushkevich ($R^2 > 0.9485$) models. The composite of nanocellulose and chitosan exhibited the highest Langmuir adsorption capacity ($301.20 \text{ mg} \cdot \text{g}^{-1}$) at 47°C after a 24 h shaking period at a dosage of $2 \text{ g} \cdot \text{L}^{-1}$ as the adsorbent and pH of 7. The adsorption of MB by the fabricated solid materials fitted well with the linear PSO ($R^2 > 0.9806$) and Elovich ($R^2 > 0.9574$) kinetic model. The enthalpy, entropy, and free energy change for the adsorption of MB onto CSC were determined to be $47.11 \text{ kJ} \cdot \text{mol}^{-1}$, $0.172 \text{ kJ} \cdot \text{mol}^{-1} \cdot \text{K}^{-1}$, and $-3.29 \text{ kJ} \cdot \text{mol}^{-1}$, respectively at 20°C . Thermodynamic investigation showed that MB adsorption is spontaneous, endothermic, favorable ($0 < R_L < 1$, $0.017\text{--}0.313$), and physisorption ($E_{\text{DR}} < 8 \text{ kJ} \cdot \text{mol}^{-1}$). Compared to the other eluents, nitric acid produced the highest desorption percentage (98.5%).

Keywords Loofah sponge · Nanocellulose · Chitosan · Methylene blue · Adsorption

1 Introduction

Recently, numerous pollutants have been released into the environment due to the rapid rise of industry, especially organic dyes, that are generated as effluents from textile, wood, and other different industries [1]. Many organic dyes are discharged into water bodies resulting in significant environmental issues. Organic colorants have been reported to be more hazardous, non-biodegradable, and persist in the environment for several years [2]. Methylene blue dye is

classified as a cationic organic dye that finds application in food, medicine, textiles, and chemical indicators [3]. It causes main health issues, like breathing difficulties, nausea, dyspnea, eye burn dermatitis, vomiting, excessive perspiration, and cyanosis [4]. Thus, the removal of MB dye is required from discharge waste effluents which is a major environmental concern [5]. Many techniques have been recently used to eliminate organic dye from effluent, including photodegradation [6], flocculation and coagulation [7], ozonation [8], advanced oxidation, electrochemical oxidation processes [9], bioremediation [10], and adsorption [11–13]. The adsorption process is the best method when compared to alternative methods [14]. It is characterized as extremely effective, eco-friendly, operation simplicity, and low in cost [15]. Some common adsorbents, such as activated carbon, zeolites, limestone, natural clay, and waste

✉ Asaad F. Hassan
asmz68@sci.dmu.edu.eg

¹ Chemistry Department, Faculty of Science, Damanhour University, Damanhour, Egypt

from industry and agriculture, were used to remove dyes from wastewater. Most adsorbents are not widely available, some are expensive, and others are ineffective as adsorbents in decontamination and water treatment [16]. Because of their special qualities, such as having more active sites and a larger surface area, nanomaterials are thought to be the ideal adsorbent [17]. Their chemical affinity for target compounds can be increased by adding different chemical groups to them [18]. Applications of nanoparticles are being investigated in the fields of medicine, food industry, pharmaceuticals, environmental remediation, and agriculture [19]. Adsorption has made use of a wide range of nanomaterials, such as carbon nanotubes, silicon nanoparticles, aerogels, nanofibers, nano clay, and polymer-based nanomaterials [20].

Cellulose with the formula $(C_6H_{10}O_5)_n$ is the most naturally rich polymer on the planet, present in wood, plant loofah sponge, sisal, coconut husk, hemp, kenaf, rice husk, algae, and bacteria. Cellulose is an intriguing biomaterial with features such as hydrophilicity, nontoxicity, biodegradability, eco-friendly, easily surface modifiable, and simplicity of modification [21]. Nanocellulose (NC) has gained recognition recently as a sustainable biomaterial with a wide range of uses in the paper industry, water treatment, food packaging, cosmetics, and agriculture, among other industries [22]. In water treatment, nanocellulose is utilized as an adsorbent to eliminate organic and inorganic pollutants from the environment by adsorption or filtration process [23]. Plant loofah sponge (LS) provides a source of cellulose. It is classified as a subtropical, non-woody plant of the Cucurbitaceae family. LS has several advantages, including a high content of cellulose (55–90%), nontoxicity, inexpensive, biodegradability, lightweight, and environmental friendliness [24]. It is utilized as a natural adsorbent in the removal of organic dyes from polluted water owing to its quick adsorption kinetics, large surface area, and excellent stability [25]. Nanocellulose is typically extracted mechanically, chemically, or enzymatically from cellulose, the most abundant polymer found in cotton linters and plant cell walls [23]. Because nanocellulose has several -OH groups, its adsorption process can be increased up by making appropriate modifications, such as adding surface groups or creating new compounds. Chitosan is a derivative of chitin, which is the second record rich natural polysaccharide on earth after cellulose, and is found in several living organisms such as crustacean shells, fungal cell walls, and arthropod exoskeletons [26]. Chitosan is a semi-synthetic polysaccharide composed of N-acetyl glucosamine and glucosamine entities [27]. Chitosan is prepared through four main steps: demineralization, discoloration, deproteinization, and deacetylation. Chitosan acts as an effective adsorbent to remove organic dyes from wastewater. It has

remarkable adsorption capacity due to having a high concentration of amino and hydroxyl groups in its molecular structure [28]. Using coordination, hydrogen bonding, and electrostatic methods, these groups produce strong interaction with contaminants. Although chitosan is ideal for the adsorption of dyes and other contaminants, it is rarely used in practical applications due to its low mechanical strength. As a result, physical or chemical alterations may improve its affinity for pollutants [29]. Adsorption efficiency can be increased further by using nanocomposites. Bi and triple nanocomposites have good features such as high adsorption capacity, high thermal stability, high specific surface area, acceptable crystallinity, extremely porous nature, easy removal after applications, and the existence of several active sites. Nanocomposites are recognized as a superior alternative for eliminating inorganic and organic contaminants from water due to their advantages [30]. Adsorption of methylene blue was investigated and applied in several previous studies using different biocomposites such as activated clay/chitosan/ZnO [31], nanohydroxyapatite/chitosan [32], and $CuMn_2O_4$ /chitosan micro/nanocomposite [33], where they achieved adsorption capacity at 17.35, 84.89, and 54.05 $mg \cdot g^{-1}$, respectively. However, the reported results achieved limited adsorption capacity towards MB due to the small surface area and other limited characteristics of their prepared biocomposites. Therefore, we synthesized a composite composed of nanocellulose extracted from LS with chitosan as a new type of biocomposite with remarkable adsorption properties to remove methylene blue from an aqueous medium.

The present work discusses the preparation of three adsorbents namely, nanocellulose (NC) that was obtained from LS by delignification using sodium hydroxide solution, chitosan pellets (CS) that was prepared from solid chitosan by using the precipitation method, and chitosan and nanocellulose (CSC) as a new biocomposite for effective removal of MB dye. The fabricated solid adsorbents were explored by FTIR, XRD, SEM, TEM, TGA, zeta potential, and N_2 adsorption techniques. The impact of solution pH, adsorbent dosage, temperature, starting adsorbate concentration, and shaking time were among the adsorption conditions examined in the study of batch adsorption of methylene blue. Thermodynamic and kinetic values were calculated to identify the type of MB adsorption and mechanism. Methylene blue desorption from CSC was carried out by via different eluant solutions, and CSC reusability was considered after seven cycles of the adsorption and desorption procedures.

2 Materials and Methods

2.1 Materials

The plant loofah sponge was collected from a farm in Damanhur, Egypt, cut into extremely small pieces, washed with distilled water for the elimination of any impurities, and then dried at 90 °C. The dried LS was milled into fine powder by Retsch ZM200 titanium mill. Chitosan and methylene blue (MB) were purchased from Sigma-Aldrich Co., St. Louis, MO, USA. While, hydrochloric acid (37%), sodium hydroxide ($\geq 98\%$), acetic acid (80%), nitric acid (70%), ethanol (98%), benzene (99%), and sodium hypochlorite (12%) were purchased from Loba. Chemie., Co., India. The chemicals were not further purified before being used.

2.2 Preparation of Solid Materials

2.2.1 Preparation of Nanocellulose from Plant Loofah Sponge (NC)

Certain weight of plant loofah powder (20 g) was mixed with 400 mL of NaOH solution (17.5% w/v) and heated for 4 h at 90 °C on a hot plate with magnetic stirring to remove lignin. The resultant mixture was filtered, rinsed with distilled water until the filtrate solution reached neutrality, and dried at room temperature for 24 h. The delignified dry plant loofah sponge was bleached using a sodium hypochlorite solution (12% w/v) at 80 °C for 1.5 h. The bleached loofah sponge was rinsed with distilled water till free from any residual alkali and dried at 50 °C. The dried bleaching product was hydrolyzed with 100 mL of hydrochloric acid (2.5 c) for 45 min at 100 °C under continuous stirring. After the hydrolyzed product had been cleaned to a neutral filtrate solution, two days of dialysis against distilled water was performed. Cellulose nanoparticles (NC) was produced as a snow-white powder [34].

2.2.2 Synthesis of Chitosan Pellets (CS)

Chitosan pellets were synthesized by dispersing 2 g of chitosan in 200 mL of (2% w/v) acetic acid under continuous stirring for 4 h. The resulting solution was slowly fallen into 2 mol. L⁻¹ NaOH solution by using a fine syringe. The precipitate that was produced was filtered, repeatedly cleaned with distilled water to remove any remaining contaminants, and then dried at 70 °C for 24 h [35].

2.2.3 Fabrication of Chitosan/Nanocellulose Composite (CSC)

Chitosan/nanocellulose composite was synthesized by mixing 1 g of solid chitosan with 100 mL of (2% w/v) of acetic acid under continuous magnetic stirring for 4 h. The extracted nanocellulose (1 g) was sonicated and suspended in 15 mL of distilled water before being added to the chitosan solution. The subsequent mixture was agitated for 2 h till homogeneous solution, then slowly added into 2 mol. L⁻¹ of sodium hydroxide by a syringe. The produced solid composite was filtered, washed by water, and dried at 70 °C for 24 h.

2.3 Characterization of the Prepared Solid Adsorbents

Physicochemical techniques were used to determine the characteristics of the constructed solid materials such as TGA (thermogravimetric analysis), XRD (X-ray diffraction spectra), nitrogen gas adsorption and desorption, SEM (scanning electron microscope), TEM (transmission electron microscopy), zeta potential, and FTIR (Fourier transform infrared spectrometer).

Thermogravimetric analysis of LS, NC, CS, and CSC solid materials was investigated at a nitrogen flow rate of 5 mL. min⁻¹ with a heating rate of 10 °C. min⁻¹ up to 800 °C by a thermal analyzer (NETZCH STA 409, Germany) apparatus.

Textural structure for NC, CS, and CSC as V_T (total pore volume), \bar{r} , nm (average pore radius), and S_{BET} , m². g⁻¹ (specific surface area) were determined by N₂ adsorption/desorption at -196 °C using a NOVA 3200e gas sorption analyzer (Quantachrome Corporation, USA).

The crystal structure for NC, CS, and CSC was investigated by XRD using (D8 advance diffractometer) at a current of 40 mA and a voltage 40 kV. The diffraction measurements for the samples were gathered from 5 to 80 (2 θ) with a scanning step 0.5°.min⁻¹ (2 θ).

Utilizing a JEOL JSM-6510LV, the SEM images for NC, CS, and CSC were investigated. The fabricated solid samples were prepared by immediately precipitating them on an aluminum carrier and then by covering them with a tiny gold film under a high vacuum and at an elevated speeding voltage of 15 kV.

The morphological structure for NC, CS, and CSC was determined by TEM using a JEOL-JEM-2100 model. Solid materials were ultrasonically dissolved in an anhydrous ethanol solution for 45 min, placed on a copper strip, and dried for 24 h before being measured.

The surface chemical functional groups for NC, CS, and CSC were investigated by using a Mattson 5000 FTIR

spectrometer between 400 and 4000 cm^{-1} (FTIR). Zetasizer Nano S, Malvern Instruments, UK was used to investigate zeta potential for NC, CS, and CSC.

2.4 Batch Adsorption of Methylene Blue

The batch (static) adsorption of methylene blue from the aqueous medium on NC, CS, and CSC was applied by incorporating 25 mL of methylene blue solution that has a certain concentration with 0.05 g of solid adsorbent at pH 7, 24 h as time of shaking at 20 °C. The clear solution was filtered utilizing Whatman filter paper. The initial ten milliliters from the filtrate were eliminated, and the remaining methylene blue concentration in the filtrate was detected at a wavelength of 662 nm by applying a UV-vis spectrophotometer. The adsorption capacity at equilibrium was estimated using Eq. 1:

$$q_e = \frac{(C_i - C_e) \times V}{m} \quad (1)$$

where the starting and final MB concentrations ($\text{mg} \cdot \text{L}^{-1}$) are denoted by C_i and C_e , respectively. V is the volume of the solution (L), and m is the adsorbent's mass (g). Varied application conditions were applied to investigate the effect of shaking time (0.25–30.00 h), pH (2–12), solid dosage (0.2–2.0 $\text{g} \cdot \text{L}^{-1}$), starting MB concentration (25–600 $\text{mg} \cdot \text{L}^{-1}$), and investigating the temperature of adsorption (20,30,40, and 47 °C). The removal (%) was estimated by Eq. 2:

$$R\% = \frac{C_i - C_e}{C_i} \times 100 \quad (2)$$

2.5 Adsorption Kinetic Models

Different kinetic models (Eqs. 3–5) were used to calculate the rate and adsorption mechanism of MB onto the prepared solid adsorbents [36].

PFO (pseudo-first order) kinetic model:

$$\ln(q_{exp} - q_t) = \ln q_{exp} - k_1 t \quad (3)$$

PSO (pseudo-second order) kinetic model:

$$\frac{t}{q_t} = \frac{1}{k_2 q_{exp}^2} + \frac{1}{q_{exp}} t \quad (4)$$

Elovich kinetic model:

$$q_t = \frac{1}{\beta} \ln \alpha \beta + \frac{\ln t}{\beta} \quad (5)$$

Adsorption capacity at a certain time (q_t , $\text{mg} \cdot \text{g}^{-1}$) was considered utilizing the next equation:

$$q_t = \frac{(C_i - C_t)}{m} \times V \quad (6)$$

Herein, k_1 (h^{-1}), k_2 ($\text{g} \cdot \text{mg}^{-1} \cdot \text{h}^{-1}$), and C_t ($\text{mg} \cdot \text{L}^{-1}$), are the PFO, and PSO rate constants model, and the equilibrium concentration of MB at time t , respectively. q_e and q_t ($\text{mg} \cdot \text{g}^{-1}$) are the quantities of MB adsorbed on the adsorbents at equilibrium and a certain time (h). α ($\text{mg} \cdot \text{g}^{-1} \cdot \text{h}^{-1}$) and β ($\text{g} \cdot \text{mg}^{-1}$) are related to the MB adsorption's initial rate and surface coverage extent, respectively.

2.6 Adsorption Isotherm Models

Different isotherms of adsorption were employed to investigate MB adsorption on the surface of all the investigated adsorbents.

2.6.1 Linear Langmuir Adsorption Model

According to the Langmuir adsorption isotherm model, the adsorbed layer is a monolayer that forms when adsorbate is adsorbed on a surface that is homogeneous in solid adsorbent. The linear Langmuir model is illustrated by Eq. 7 [37].

$$\frac{C_e}{q_e} = \frac{1}{b q_m} + \frac{1}{q_m} C_e \quad (7)$$

The Langmuir adsorption constant, equilibrium concentration, maximum adsorption capacity, and adsorption capacity at equilibrium are denoted by the variables b ($\text{L} \cdot \text{mg}^{-1}$), C_e ($\text{mg} \cdot \text{L}^{-1}$), q_m ($\text{mg} \cdot \text{g}^{-1}$), and q_e ($\text{mg} \cdot \text{g}^{-1}$), respectively. The nature of methylene blue adsorption was determined by the dimensionless separation factor R_L value. If it is favorable ($0 < R_L < 1$), irreversible ($R_L = 0$), and unfavorable ($R_L > 1$). The following equation was used to determine the dimensionless separation factor:

$$R_L = \frac{1}{1 + b C_i} \quad (8)$$

2.6.2 Freundlich Adsorption Model

the reversibility of the adsorption process and multilayer adsorption on heterogeneous solid adsorbent surfaces are addressed by the Freundlich isotherm model [38]. The linear Freundlich model is calculated by Eq. 9

$$\ln q_e = \ln K_F + \frac{1}{n} \ln C_e \quad (9)$$

Herein, n and K_F ($\text{L}^{1/n} \cdot \text{mg}^{1-1/n} \cdot \text{g}^{-1}$) are the Freundlich coefficients that represent adsorption intensity and adsorption capacity, respectively.

2.6.3 Temkin Adsorption Model

The Temkin isothermal equation is applicable to measure the heat of adsorption when increasing the adsorbed surface coverage is expected to diminish the adsorption heat for all molecules. The linear Temkin model is applied by Eq. 10 [39].

$$q_e = \beta \ln K_T + \beta \ln C_e \quad (10)$$

$$\beta = \frac{RT}{b_T} \quad (11)$$

Where β is the adsorption heat constant, R ($8.314 \text{ J} \cdot \text{mol}^{-1} \cdot \text{K}^{-1}$) is the gas constant, K_T ($\text{L} \cdot \text{g}^{-1}$) is constant related to Temkin isotherm, T is the absolute temperature with kelvin, and b_T ($\text{J} \cdot \text{mol}^{-1}$) is the constant of Temkin model.

2.6.4 Adsorption Model of Dubinin-Radushkevich

The Dubinin-Radushkevich (D-R) isotherm is employed to distinguish between the adsorption of MB on heterogeneous and homogeneous solid surfaces. The linear D-R model is determined by Eq. 12

$$\ln q_e = \ln q_{DR} - K_{DR} \epsilon^2 \quad (12)$$

$$\epsilon = RT \ln \left(1 + \frac{1}{C_e} \right) \quad (13)$$

Herein, K_{DR} ($\text{mol}^2 \cdot \text{kJ}^{-2}$), ϵ , q_{DR} ($\text{mg} \cdot \text{g}^{-1}$), and T are represented by the activity coefficient, Polanyi potential, the maximum adsorption capacity, and the absolute temperature with kelvin respectively. The mean adsorption energy (E_{DR} , $\text{kJ} \cdot \text{mol}^{-1}$) is calculated by the following equation:

$$E_{DR} = \frac{1}{\sqrt{2K_{DR}}} \quad (14)$$

2.7 Thermodynamic Parameters of MB Dye

Thermodynamic parameters are used to examine the spontaneity, ability, and heat of methylene blue adsorption by the produced adsorbents. These parameters include the change

of free energy (ΔG°), entropy (ΔS°), and enthalpy (ΔH°) [40]. The parameters of thermodynamics were calculated by the following equations:

$$\ln K_d = \frac{\Delta S^\circ}{R} - \frac{\Delta H^\circ}{RT} \quad (15)$$

$$K_d = \frac{C_s}{C_e} \quad (16)$$

$$\Delta G^\circ = \Delta H^\circ - T \Delta S^\circ \quad (17)$$

where the values of ΔS° ($\text{kJ} \cdot \text{mol}^{-1} \cdot \text{K}^{-1}$) and ΔH° ($\text{kJ} \cdot \text{mol}^{-1}$) were obtained using the Van't Hoff plot's slope and intercept (Eq. 15). R and k_d are constants related to the gas adsorption constant and the adsorption distribution equilibrium. C_s and C_e ($\text{mg} \cdot \text{L}^{-1}$) are the concentration of methylene blue on the adsorbent surface and the equilibrium solution concentration.

2.8 Desorption of Methylene Blue and the Reusable Nature of Solid Adsorbent

Methylene blue desorption was investigated by mixing 0.5 g of CSC with 100 mL ($500 \text{ mg} \cdot \text{L}^{-1}$) of methylene blue solution and continuous shaking for 24 h. After reaching the adsorption equilibrium, the CSC was filtered, gently washed with distilled water to get rid of any leftover MB, and dried at 35°C . Methylene blue pre-loaded CSC (0.1 g) was mixed with 50 mL of different selected desorption solutions such as distilled water, ethanol, benzene, sodium hydroxide, and nitric acid. After that, the solution was shaken for 24 h at 20°C . After filtering, the amount of desorbed dye in the solution was calculated. Desorption efficiency (%) was calculated by Eq. 18 [41].

$$\text{Desorption efficiency (\%)} = \frac{V \times C_d}{m \times q} \times 100 \quad (18)$$

The volume of the desorbing agent, the concentration of the dye in solution following desorption from the CSC surface, the maximum adsorption capacity, and the mass of the solid adsorbent are denoted by the letters V (L), C_d ($\text{mg} \cdot \text{L}^{-1}$), q ($\text{mg} \cdot \text{g}^{-1}$), and m (g), respectively.

Throughout seven cycles of methylene blue adsorption/desorption procedures, the reusability of the adsorbent was examined. The dye was adsorbed by CSC at $600 \text{ mg} \cdot \text{L}^{-1}$ concentration of dye, $\text{pH}=7$, adsorbent dosage of $2 \text{ g} \cdot \text{L}^{-1}$, 24 h of shaking time, and at room temperature. After each adsorption cycle, the solid adsorbent was filtered, rinsed with distilled water, and repeatedly washed with 35 mL of

HNO_3 (0.03 mol. L^{-1}) to desorb the pre-adsorbed MB. It was then dried at 75 °C for the next use.

3 Results and Discussion

3.1 Solid Material Characterization

Thermogravimetric analysis (TGA) was used to determine the thermal stability of the produced solid adsorbents at temperatures as high as 800 °C where TGA for LS, NC, CS, and CSC are displayed in Fig. 1a. There are three stages to the decomposition of LS. The first step happens at a temperature of up to 110 °C and involves a 4.7% mass loss due to surface adsorbed water molecules have been eliminated. The second step from 120 to 200 °C shows a mass loss of 11.0% for LS. The relatively small mass loss in this stage is due to the evaporation of internal sorbed water molecules. The third stage occurs above 230 °C with a higher mass loss of about 68.4%. The significant mass loss is thought to be caused by the decomposition of lignin and cellulose at this stage [42]. NC thermally decomposes over two stages; the early stage is at a temperature lower 240 °C with a mass loss of 6.4%. This is caused by the depletion of water and some volatile simple components. Finally, the second stage occurs

above 250–380 °C with mass loss of about 82.5% due to the dehydration, depolymerization of cellulose associated with the simultaneous formation of CO_2 , H_2O , CO , and charcoal, and breaking down of glycosyl units [43]. TGA curves for CS and CSC, as illustrated in Fig. 1a, typically exhibited two stages of mass loss. The first step, which happened at temperatures up to 150 °C, can be connected to the external and internal adsorbed moisture molecules. The second stage is up to 800 °C with mass loss of 48.90 and 55.84% for CS and CSC, respectively. It is related to polymerization, the breaking down of the polysaccharide backbone, and the destruction of acetylated and deacetylated units [44]. These results revealed that CSC has greater thermal stability than LS and NC but lower than CS.

For solid adsorbents, textural properties including specific surface area, pore radius, and total pore volume are important. The nitrogen adsorption isotherms of NC, CS, and CSC are shown in Fig. 1b. All solid samples showed type II adsorption isotherms, which confirms that mesopores are present within each sample, by the IUPAC classification. Furthermore, all samples except CS exhibited hysteresis loops of the H3 type considered to be features of slit-like pores due to nanoparticle aggregation [34]. Considering the findings listed in Table 1, the specific surface area and total pore volume of $\text{CSC} > \text{CS} > \text{NC}$ ($639.3 > 184.9 > 66.7 \text{ m}^2$).

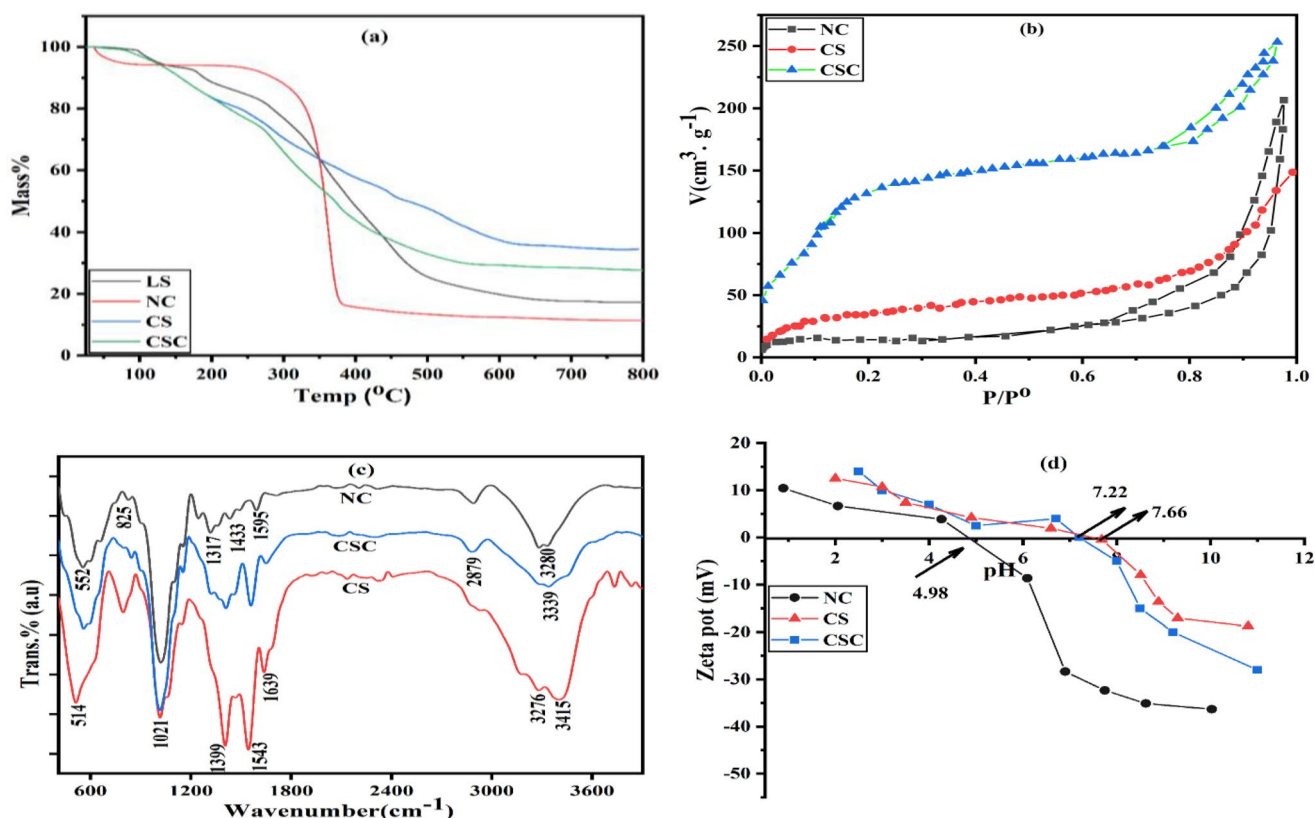


Fig. 1 TGA curves (a) for LS, NC, CS, and CSC. Nitrogen adsorption/desorption isotherms (b), FTIR curves (c), and zeta potentials (d) for NC, CS, and CSC

g^{-1} and $3.066 > 0.196 > 0.154 \text{ cm}^3 \cdot \text{g}^{-1}$, respectively) where the surface area of CSC more than that for CS and NC by 3.5 and 9.5 times, respectively. The previous result indicates that CSC is a highly porous nanocomposite material. The porous structure of CSC proves its advanced capability as an adsorbent for organic molecule adsorption. The mesoporous nature (\bar{r} , 2.012–4.619 nm) of the prepared adsorbents allowed MB to diffuse into the pores more easily [20].

The phase and crystalline structure of NC, CS, and CSC were determined by XRD analysis as illustrated in Fig. S1. X-ray diffraction patterns for NC exhibited three main diffraction peaks at 2θ of 15.4° , 22.5° , and 34.5° in contrast to planes 110, 200, and 004, respectively, and they have been linked to cellulose type I. The peak at 22.5° was discovered to be sharper than the other peaks, confirming that the cellulose crystal lattice in the (200) plane was ideal. The spectra at 15.4° (110) and 34.5° (004) plane reflection indicated lignin and hemicellulose elimination from the plant loofah sponge, resulting in a higher crystallinity index. The prepared NC is pure due to the absence of any peaks that can be recognized [45]. CS revealed three next peaks: the first and second peaks were identified at 2θ of 15.1° and 33.7° , indicating a highly amorphous region, while the third peak was identified in a sharp form at 2θ of 22.0° , indicating chitosan crystallinity [46, 47]. In the case of CSC, the characteristic broad peak of CS at 2θ of 15.1° shifted to a higher value with the addition of cellulose ($2\theta = 15.7^\circ$) for the chitosan-nanocellulose composite. This pattern demonstrated the benefit of the interaction between the two biopolymers [48].

The reported FTIR curves of NC, CS, and CSC are shown in Fig. 1c for determining their surface chemical functional groups. The peak for NC at 825 cm^{-1} is due to cellulose C-H stretching. Bands at 1317 and 1433 cm^{-1} are connected to (H-C-H) symmetric bending groups, which are common for polysaccharides. There are no recognized peaks about 1740 cm^{-1} that belong to hemicellulose, indicating the purity of the NC structure. In addition, the peak at 1595 cm^{-1} corresponded to C=C vibration in an aromatic ring [49]. The peak at $552\text{--}657 \text{ cm}^{-1}$ indicates the presence of an out-of-plane bending vibration of the C-OH groups, confirming the typical cellulose construction with β -glycosidic bonds of the glucose ring inside the structure. The peak is at 3280 cm^{-1} for NC due to -OH stretching vibration [46]. Chitosan has peaks at 3276 and 3415 cm^{-1} that are attributed to N-H stretching and O-H vibration, respectively. The

characteristic bands for chitosan appear at 1639 , 1543 , and 1399 cm^{-1} that are associated with C=O (amide I), N-H bending vibration (amide II), and C-N stretching (amide III), respectively. The peak at 1021 cm^{-1} for all samples is referred to as glycosidic linkage [50]. The vibrations of the -NH and C=O groups in chitosan are represented by the exhibited peaks at 514 and 576 cm^{-1} [51]. The peaks at 2879 cm^{-1} revealed that there are both asymmetric and symmetric stretching vibrations in the CSC composite. A comparison of the FTIR measurements with chitosan shows 3276 cm^{-1} moved to a new frequency of 3339 cm^{-1} . This chemical shift shows that an intermolecular collision between the OH and NH groups of cellulose and chitosan occurred throughout the reaction, indicating good interaction between them [48, 52].

The zeta potential for nanocellulose, chitosan, and chitosan/nanocellulose composite at various pH values are shown in Fig. 1d. The observations of zeta potential values for NC, CS, and CSC indicated pH_{PZC} values at 4.98, 7.66, and 7.22, respectively, as presented in Table 1. This means that at $\text{pH} < \text{pH}_{\text{PZC}}$, all solid surfaces have a positive charge, while at $\text{pH} > \text{pH}_{\text{PZC}}$, all solid surfaces have a negative charge.

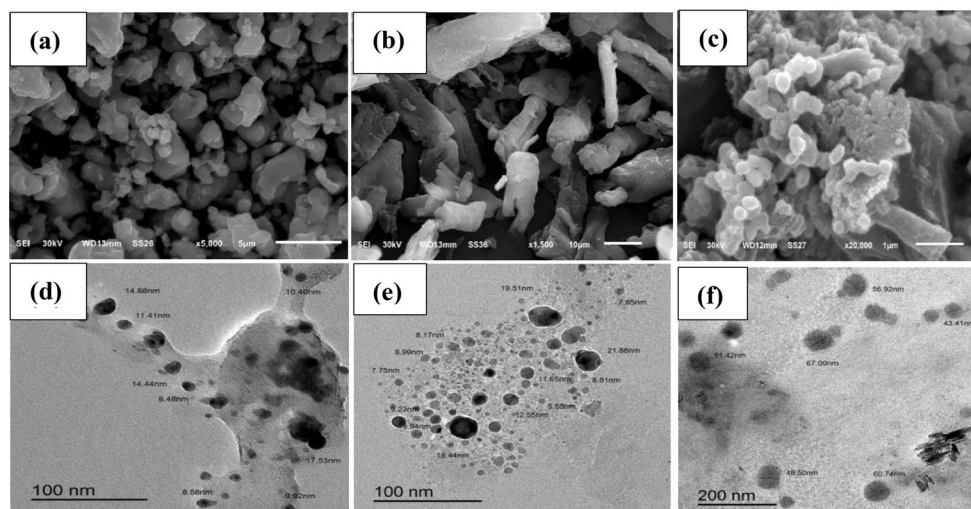
The surface morphology and shape of NC, CS, and CSC samples were determined by SEM analysis as presented in Fig. 2a-c. The morphology of nanocellulose resulting from the alkaline and bleaching treatments is depicted in Fig. 2a, where the surface of nanocellulose accidentally becomes rougher with consistent porosity nano-scale with uniformly dispersed single crystalline particles. Impurities like lignin and hemicellulose were largely eliminated from the surface of NC due to the chemical treatments. This confirms the effectiveness of the applied treatment procedures [53]. The CS image displayed an irregular structure with a non-porous surface, smooth, as well as some irregular patterns and membrane gaps. Chitosan/nanocellulose composite formed a stronger network than chitosan beads. It can be explained by the strong attachment between chitosan and nanocellulose by strong hydrogen bonds and the building of a thick skeleton through preparation. This feature could give the produced composites better chemical and mechanical properties than native cellulose [48].

TEM images of NC, CS, and CSC are depicted in Fig. 2d-f, respectively, which agree with SEM studies in size and shape. The TEM image for NC showed a spherical shape. The structure and properties of NC are affected by different factors, including the cellulose source and the method of extraction. Accumulation in NC has been related to the evaporation of water, the small size of nanocellulose particles, and the higher surface area, which caused them to assemble via Van der Waals forces [54]. The average particle size for NC and CS is 17.3 and 12.5 nm, respectively,

Table 1 Characterization parameters for the synthesized solid adsorbents

Samples	pH_{PZC}	S_{BET} ($\text{m}^2 \cdot \text{g}^{-1}$)	V_{T} ($\text{cm}^3 \cdot \text{g}^{-1}$)	\bar{r} (nm)	TEM Average P_s (nm)
NC	4.98	66.7	0.154	4.619	17.3
CS	7.66	184.9	0.196	2.120	12.5
CSC	7.22	639.3	0.366	2.012	51.8

Fig. 2 SEM (a–c) and TEM images (d–f) for NC, CS, and CSC, respectively



but when CS was mixed with NC, the average size increased to approximately 51.8 nm for CSC.

3.2 Batch Adsorption of MB

3.2.1 Influence of Adsorbent Dose

Figure 3a illustrates the relationship between solid dosage (g. L^{-1}) and the adsorption capacity (q_e , Eq. 1) using 0.2–2.0 g. L^{-1} as the range of adsorbent dosage, 50 mL (600 mg. L^{-1}) of MB solution at $\text{pH}=7$, 20 °C, and after 24 h as time of shaking. As demonstrated in Fig. 3a, increasing the adsorbent dosage from 0.2 to 1.4 g. L^{-1} causes an increase in adsorption capacity from 9.9, 29.9, and 44.8 to 55.8, 42.7, and 59.8 mg. g^{-1} by 5.6, 1.4, and 1.3 times for NC, CS, and CSC, respectively.

This is mostly due to a rise in the active sites of adsorbents when adsorbent dosage increases. Only a 0.4–4.7 mg. g^{-1} increase was detected at the adsorbent dosage of 1.4 to 2.0 g. L^{-1} . At dosages greater than 2.0 g. L^{-1} , there was no obvious rise in MB removal, indicating that the adsorption process had reached saturation. The optimum adsorbent dosage of 2.0 g. L^{-1} was chosen for NC, CS, and CSC based on earlier findings.

3.2.2 Effect of pH

Initial adsorbate solution pH values affect not only the state of surface-group adsorbents but also the adsorbate state. The effect of pH was investigated by several methylene blue solutions prepared at various pH values (2–12) with 50 mL (600 mg. L^{-1}) and 0.1 g of adsorbent at 20 °C for 24 h as shaking time. The pH of the solutions was modified with 0.1 M NaOH and 0.05 M HCl solutions. Figure 3b shows that by increasing pH values from (2–12), the adsorption capacity for adsorbents increases, where q_e increases from

15.6, 23.8, and 39.9 mg. g^{-1} to 56.4, 47.9, and 65.1 mg. g^{-1} for NC, CS, and CSC, respectively. This is related to the fact that methylene blue generates positive ions. pH has an impact on the adsorbent's charge; at a higher pH ($\text{pH} > \text{pH}_{\text{pzc}}$), solid adsorbents (NC, CS, and CSC) gain negative charges at their surface, which leads to a rise in electrostatic attraction between negatively charged adsorbent surfaces and MB cation dye. Conversely, at lower pH ($\text{pH} < \text{pH}_{\text{pzc}}$), an increasing positive charge on the adsorbent surface leads to electrostatic repulsion with the methylene blue dye [55]. According to the prior result, the adsorption efficiency improved in a more basic medium and decreased in a more acidic medium based on the pH_{pzc} (4.98, 7.66, and 7.22) for NC, CS, and CSC, respectively. The structural flexibility of chitosan promotes it to rapidly transition from a positively charged ($-\text{NH}_3^+$) to neutral ($-\text{NH}_2$) state in circumstances ranging from acidic to extremely basic medium, which causes a modest loss in capacity in both chitosan and CSC composite [56]. Thus, from pH 10–12, this reduces the ability of solid adsorbents to bind methylene blue which creates a decrease in adsorption capability.

3.2.3 Effect of Contact Shaking Time and Kinetic Data

The most suitable time of adsorption was established by graphing contact time (h) against the capacity of adsorption (mg. g^{-1}) at 20 °C within 0.25–30 h as shown in Fig. 3c. The capacity of MB adsorption by NC, CS, and CSC increased rapidly by 1.3, 1.2, and 5.3 times, respectively within the first 15 h (equilibrium time), increased just slightly from 15 to 20 h, and remained stable from 20 to 30 h. The MB adsorption process is quite fast at the beginning, which is explained by the abundance of free sites on the surface of the adsorbents. However, as the number of free sites reduces, adsorption becomes slower and unchanged, indicating that the free sites have been saturated [57]. Figure 3d–f depicts

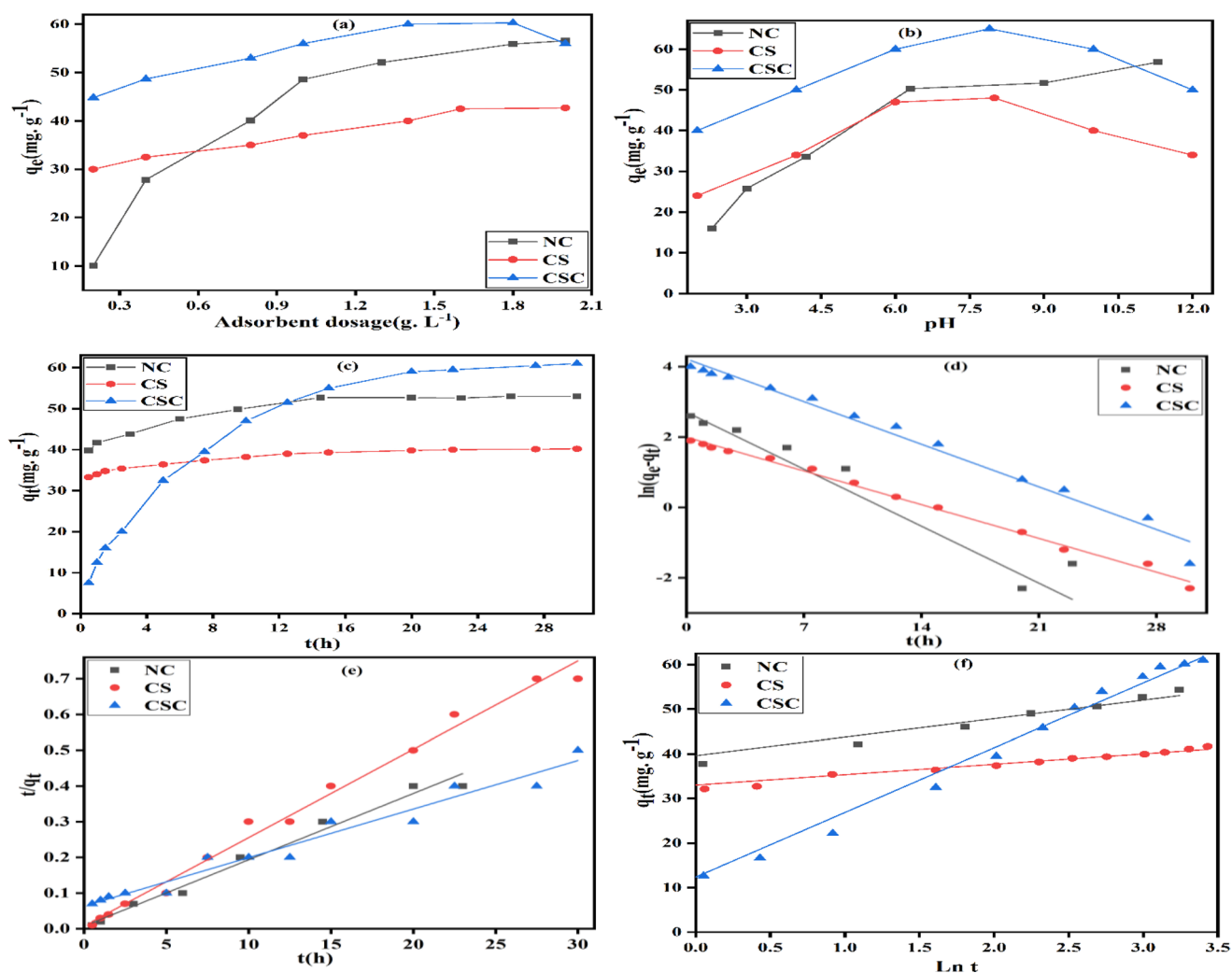


Fig. 3 Effect of nanosolid dose (a) at pH7, effect of pH (b) using adsorbent dose of $2 \text{ g} \cdot \text{L}^{-1}$, shaking time (c), PFO (d), PSO (e), and Elovich (f) plots for the MB adsorption onto NC, CS, and CSC at initial MB of $600 \text{ mg} \cdot \text{L}^{-1}$ and $20 \text{ }^\circ\text{C}$

PFO (Eq. 3), PSO (Eq. 4), and Elovich (Eq. 5), in addition to kinetic parameters presented in Table 2. As shown in the results in Table 2, the adsorption of MB is a well-fitted PSO kinetic model, as indicated by the higher correlation coefficients (R^2) (0.9806–0.9892) and relatively low variances between the Langmuir adsorption capacity (q_m) and experimental adsorption capacity (q_{exp}) values (3.8, 2.5, and 2.0% for NC, CS, and CSC, respectively). (ii) The PFO kinetic model was proven to be inadequate for estimating methylene blue adsorption on the manufactured materials due to a high disparity (16.2–84.9%) between the q_m and q_{exp} values and it also had lower R^2 values (0.8420–0.9003) when compared to the PSO. (iii) The values of rate constants (k_2 , $\text{g} \cdot \text{mg}^{-1} \cdot \text{h}^{-1}$) for PSO indicate the adsorption rate for $\text{CS} > \text{NC} > \text{CSC}$. The higher rate constant for CS is due to the stronger attraction force between the cationic MB dye and the chemical functional groups on its solid surface. (iv) Correlation coefficients (R^2) of the Elovich kinetic model

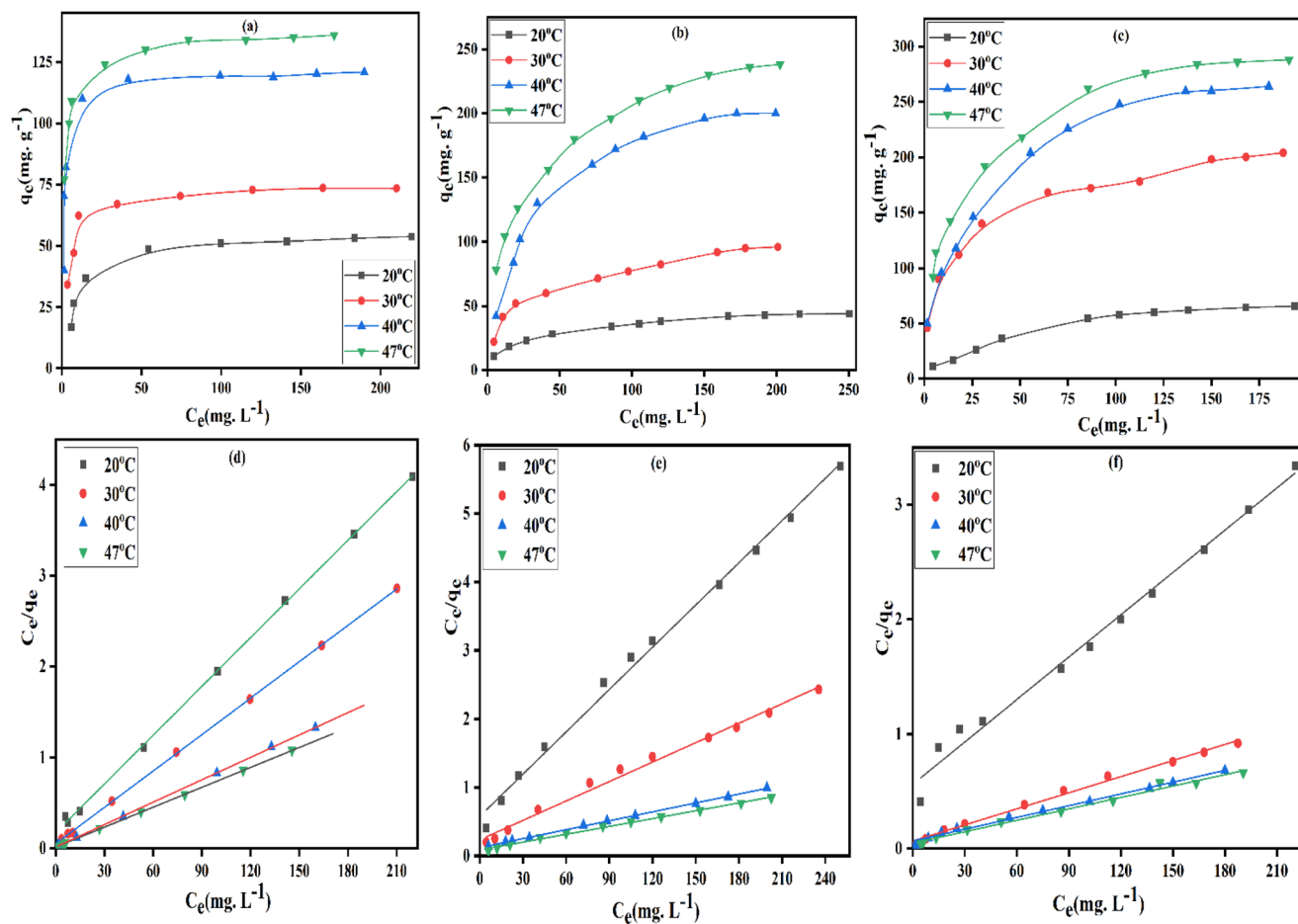
are greater than 0.9574, indicating the good applicability of that model. The values of the initial rate (α) for methylene blue adsorption perform the sequence $\text{CSC} > \text{NC} > \text{CS}$, demonstrating a rise in adsorption capacity, while β series $\text{CS} > \text{NC} > \text{CSC}$ confirmed the extent of surface coverage onto CS.

3.2.4 Effect of Primary MB Concentration

Methylene blue adsorption onto the surface of NC, CS, and CSC at 20, 30, 40, and $47 \text{ }^\circ\text{C}$ using 0.1 g of adsorbent dosage, pH 7, 24 h of contact shaking time, and 25–600 $\text{mg} \cdot \text{g}^{-1}$ as an initial concentration of MB are displayed in Fig. 4a-c. Increasing MB concentration facilitates dye transport from the solution to the adsorbent surface, enhancing the forces of attraction between adsorbent surface sites and MB molecules. Figure 4a-c illustrates the adsorption capacity (q_e , $\text{mg} \cdot \text{g}^{-1}$) of MB sharply raised at the beginning at a lower

Table 2 PFO, PSO, and Elovich models for MB adsorption onto NC, CS, and CSC in addition to the estimated thermodynamic parameters (adsorbent dose of 2 g. L⁻¹, 600 mg. L⁻¹, and pH 7)

Models	Parameters	NC	CS	CSC
PFO	q_m (mg. g ⁻¹)	55.93	48.64	81.17
	q_{exp} (mg. g ⁻¹)	15.02	7.36	68.02
	k_1 (h ⁻¹)	0.231	0.137	0.173
	R^2	0.8420	0.8940	0.9003
PSO	q_{exp} (mg. g ⁻¹)	53.82	47.44	79.53
	$k_2 \times 10^{-3}$ (g. mg ⁻¹ . h ⁻¹)	45.97	75.88	2.91
	R^2	0.9814	0.9892	0.9806
Elovich	α (mg. g ⁻¹ . h ⁻¹)	58.3334	32.9663	63.9891
	β (g. mg ⁻¹)	0.2412	0.4289	0.0689
	R^2	0.9574	0.9782	0.9833
Thermodynamic parameters	R^2	0.9627	0.9654	0.9722
	ΔH° (kJ. mol ⁻¹)	52.01	47.36	47.11
	ΔS° (kJ. mol ⁻¹ .K ⁻¹)	0.193	0.169	0.172
	$-\Delta G^\circ$ (kJ. mol ⁻¹)			
		20 °C	4.53	2.16
	30 °C	6.47	3.85	5.01
	40 °C	8.40	5.54	6.73
	47 °C	9.75	6.72	7.93

**Fig. 4** Adsorption isotherms of MB (a-c) and linear Langmuir plots (d-f) for NC, CS, and CSC at 20, 30, 40, and 47 °C, (2 g. L⁻¹ adsorbent dosage, pH 7, 24 h as shaking time, and 25–600 mg. L⁻¹ as the initial concentration of MB)

initial MB concentration owing to the abundance of free adsorption sites for MB molecules as adsorbate, but began to decline at higher initial concentrations due to adsorption site saturation. The adsorption isotherm model reports were studied using Eqs. 7, 9, 10, and 12 as displayed in Table 3.

The higher estimated correlation coefficients (0.9872–0.9998) reveal the perfect fitting of the Langmuir model for MB adsorption on all the produced adsorbents as illustrated in Fig. 4d-f. As shown in the results in Table 3, the adsorption capacity of CSC > CS > NC by 13.1 and 54.6% respectively, compared with CSC at 47 °C is related to increasing functional groups on the CSC surface, in addition to its advanced surface area. The increase in adsorption capacity as temperature increased from 20 to 47 °C confirms the endothermic nature of the adsorbed MB onto NC, CS, and CSC. Langmuir constant (b , L. mg^{-1}) values were detected in the category NC > CSC > CS at 47 °C as shown in Table 3, indicating a high affinity of the methylene blue dye to the adsorption sites of NC at 47 °C [58]. The dimensionless separation factor (R_L) values in this investigation range from 0.017 to 0.313, indicating that MB adsorption onto the produced adsorbent is favorable. As seen in Figs. S2 a-c and Table 3, the Freundlich isotherm depicts how adsorbate molecules interact with heterogeneous surfaces. Based on the value of the correlation coefficients (0.6620–0.9192), it is obvious that this model does not fit the equilibrium data well when compared to Langmuir isotherm. The value of $1/n$, which varies from 0 to 1, reflects the degree of linearity between solution concentration and adsorption, and also, the smaller the $1/n$, the more heterogeneity. The value of adsorption intensity (n) determines both the favorability and the character of the adsorption process. If $n > 1$, adsorption is physical. If $n < 1$, adsorption is chemical. According to the data in Table 3, The computed $1/n$ values are less than one and varied from 0.106–0.501, showing the effective and physical adsorption process of MB on adsorbents [59].

Figure 5a-c depicts Temkin plots for MB adsorption onto NC, CS, and CSC at 20, 30, 40, and 47 °C. Temkin isotherm parameters are reported in Table 3. The Temkin model perfectly fits the MB adsorption data of all solid adsorbents, as confirmed by higher R^2 values (0.9668 to 0.9989). The increased computed K_T values with increasing temperature from 20 to 47 °C demonstrate the endothermic favorable adsorption behavior onto the prepared samples [60]. The lower Temkin constant (b_T) values for NC, CS, and CSC located between 54.74 to 329.88 J. mol^{-1} ($b_T < 8 \text{ kJ. mol}^{-1}$), demonstrating the physical adsorption of methylene blue onto the solid adsorbent. Adsorbates connect to the adsorbent via weak Van der Waals interactions in the physisorption process, which is linked with relatively low adsorption energies [61].

Figure 5d-f depicts linear plots of the Dubinin-Radushkevich (D-R) model for MB adsorption onto solid adsorbents at various temperatures with data summarized in Table 3. The Dubinin-Radushkevich model distinguishes chemical and physical adsorption on heterogeneous and homogeneous surfaces utilizing adsorption means energy (E_{DR} , kJ. mol^{-1}). Furthermore, based on this model, $E_{DR} < 8 \text{ kJ. mol}^{-1}$ indicates physical adsorption and $8 < E_{DR} < 16 \text{ kJ. mol}^{-1}$ reveals chemical adsorption. The calculated E_{DR} (kJ. mol^{-1}) values in Table 3 are less than 8.0 kJ. mol^{-1} ranging between 0.1972 and 0.8612, which proves the physical adsorption of MB onto the studied solid adsorbents. The higher correlation coefficients (R^2) ranged between (0.9485–0.9987), demonstrating the best applicability of the Dubinin-Radushkevich isotherm [62, 63]. Based on the correlation coefficients, Langmuir > Temkin > Dubinin-Radushkevich > Freundlich for demonstrating MB adsorption onto the examined solid adsorbents. According to these results, the Langmuir isotherm model is the best-applied model for the adsorption of MB onto the surface of solid adsorbents.

3.2.5 Thermodynamic Parameters

The parameters of thermodynamics such as enthalpy change (ΔH°) and entropy change (ΔS°) were calculated from Van't Hoff equation (Eq. 15, Fig. 6a), whereas ΔG° was calculated from Eq. 17, and these parameters are reported in Table 2. (i) The endothermic MB adsorption nature of NC, CS, and CSC is supported by the positive values of ΔH° (47.11–52.01 kJ. mol^{-1}). (ii) The positive ΔS° value range from 0.169–0.193 indicates the affinity of MB ions for NC, CS, and CSC and suggests the disorder at the solid/solution interface increases during dye adsorption. (iii) The negative values of free energy indicate the methylene blue adsorption on the adsorbents was spontaneous [58]. (iv) The calculated values of ΔG° ranged between -2.16 to -9.75 kJ. mol^{-1} , corresponding to physical adsorption, where ΔG° for the physisorption ranged from -20 to 0 kJ. mol^{-1} while the free energy value for the chemisorption ranged from -80 to -400 kJ. mol^{-1} [60]. (v) The higher R^2 correlation coefficient of the Van't Hoff plot (> 0.9627) shows that the Van't Hoff model was well applied.

3.3 Desorption Studies and the Reusability

Figure 6b shows the desorption efficiency (D.E%) of MB from the CSC surface as determined by Eq. 18 using various solutions. The desorption efficiency for nitric acid, ethanol, benzene, sodium hydroxide, and distilled water was determined to be 98.5, 32.0, 28.0, 18.0, and 12.0%, respectively. Nitric acid is the best solvent for pre-adsorbed

Table 3 Langmuir, Freundlich, Temkin, and D-R data for the adsorption of MB onto NC, CS, and CSC (pH7, 2 g L⁻¹ as adsorbent dosage, 24 h, 20, 30, 40, and 47 °C)

Parameters	NC					CS					CSC					
	20 °C	30 °C	40 °C	47 °C	20 °C	30 °C	40 °C	47 °C	20 °C	30 °C	40 °C	47 °C	20 °C	30 °C	40 °C	47 °C
	<i>Langmuir</i>															
q_m (mg g ⁻¹)	55.93	74.96	121.51	136.80	48.64	105.71	230.41	261.78	81.17	213.22	292.40	301.20	81.17	213.22	292.40	301.20
b (L mg ⁻¹)	0.1038	0.2616	0.5648	0.5203	0.0356	0.0401	0.0351	0.0439	0.0219	0.0714	0.0514	0.0699	0.0219	0.0714	0.0514	0.0699
R_L	0.088	0.037	0.017	0.019	0.219	0.199	0.221	0.186	0.313	0.123	0.163	0.125	0.313	0.123	0.163	0.125
R^2	0.9993	0.9998	0.9998	0.9998	0.9940	0.9899	0.9990	0.9954	0.9872	0.9931	0.9925	0.9892	0.9872	0.9931	0.9925	0.9892
<i>Freundlich</i>																
$1/n$	0.264	0.158	0.152	0.106	0.346	0.339	0.427	0.318	0.501	0.296	0.364	0.302	0.501	0.296	0.364	0.302
K_F (L ^{1/n} mg ^{1-1/n} g ⁻¹)	14.4	34.4	59.2	82.5	7.1	16.4	24.0	46.8	5.1	45.89	43.9	64.1	5.1	45.89	43.9	64.1
R^2	0.8071	0.7480	0.6620	0.8813	0.8862	0.8503	0.8382	0.9000	0.9000	0.9153	0.9192	0.9101	0.9000	0.9153	0.9192	0.9101
<i>Temkin</i>																
K_T (L g ⁻¹)	7.28	36.23	44.53	54.05	3.97	4.18	4.81	5.25	1.78	2.65	10.82	12.56	1.78	2.65	10.82	12.56
b_T (J mol ⁻¹)	329.88	319.21	309.04	300.98	219.23	177.78	87.01	75.44	90.88	78.98	55.75	54.74	90.88	78.98	55.75	54.74
R^2	0.9973	0.9926	0.9892	0.9892	0.9786	0.9873	0.9854	0.9976	0.9668	0.9989	0.9875	0.9963	0.9668	0.9989	0.9875	0.9963
<i>Dubinin-Radushkevich</i>																
q_{DR} (mg g ⁻¹)	46.15	74.75	112.21	131.91	41.38	90.97	193.62	213.20	74.23	185.12	250.28	299.51	74.23	185.12	250.28	299.51
E_{DR} (kJ mol ⁻¹)	0.3788	0.4671	0.7479	0.8612	0.1972	0.2263	0.3930	0.4379	0.3885	0.4302	0.4579	0.5192	0.3885	0.4302	0.4579	0.5192
R^2	0.9636	0.9987	0.9836	0.9929	0.9605	0.9552	0.9663	0.9485	0.9586	0.9523	0.9654	0.9939	0.9586	0.9523	0.9654	0.9939

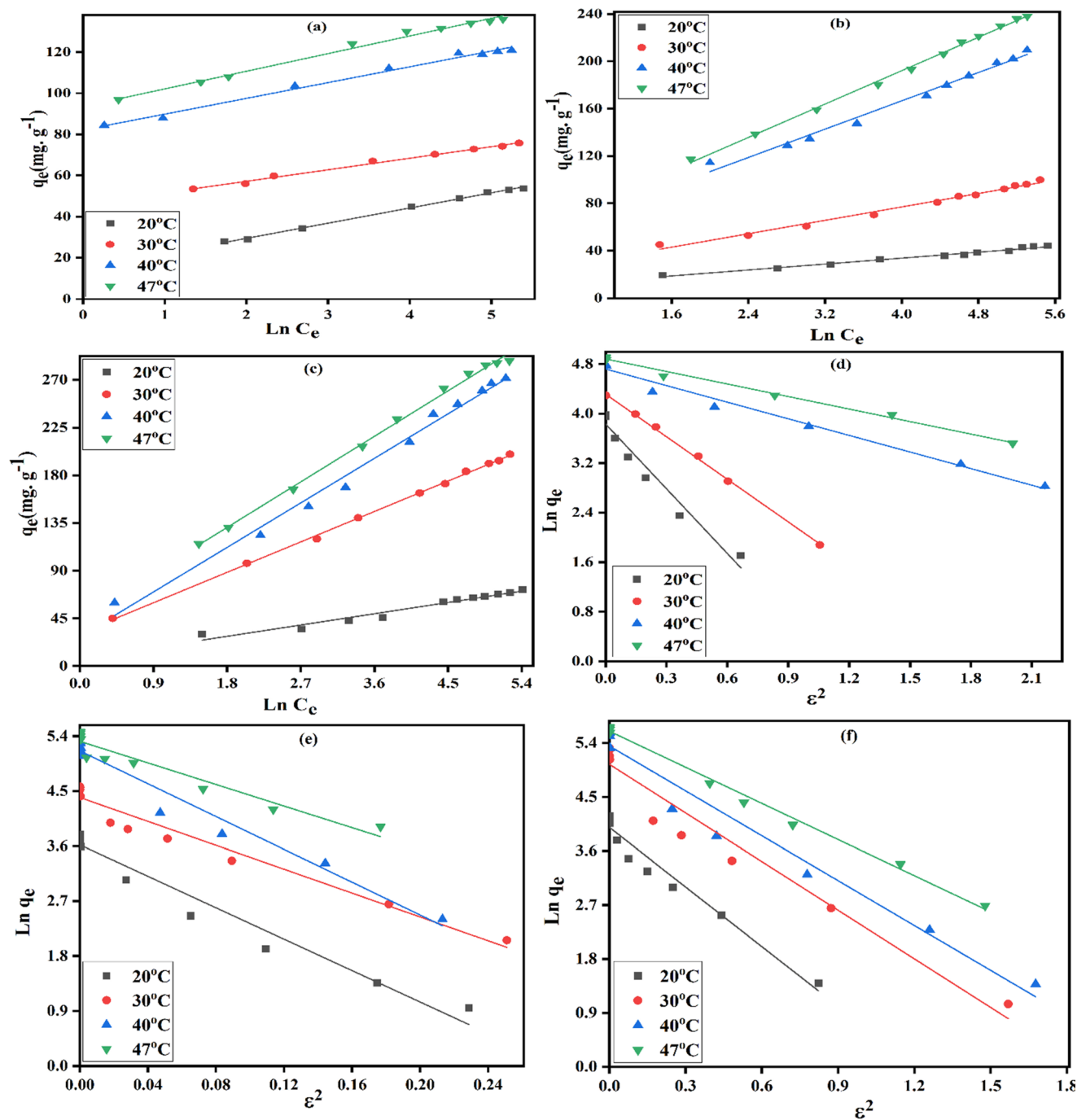


Fig. 5 Linear Temkin (a-c) and D-R (d-f) plots for adsorption of MB onto NC, CS, and CSC, respectively at 20, 30, 40, and 47 °C (pH 7, 2 g. L⁻¹ of adsorbent dose, 24 h as shaking time, and 25–600 mg. L⁻¹ as the MB initial concentration)

MB, while sodium hydroxide and distilled water showed the lowest desorption efficiency percent. The electrostatic repulsion between the MB and the CSC surface in the presence of nitric acid increases due to competing with cationic methylene blue onto the CSC surface, which is caused by the increased polarity and acidity of the inorganic solvent, which produces more protons in solution.

The reusability of CSC was examined after seven cycles of methylene blue adsorption as illustrated in Fig. 6c. CSC is reusable even after seven cycles of the adsorption/desorption process with just 6.2% of its adsorption effectiveness decreasing. Coagulation of solid adsorbent particles can result in a decrease in specific surface area and the anticipated removal of some surface chemical functional groups, which can lower adsorption efficiency [34].

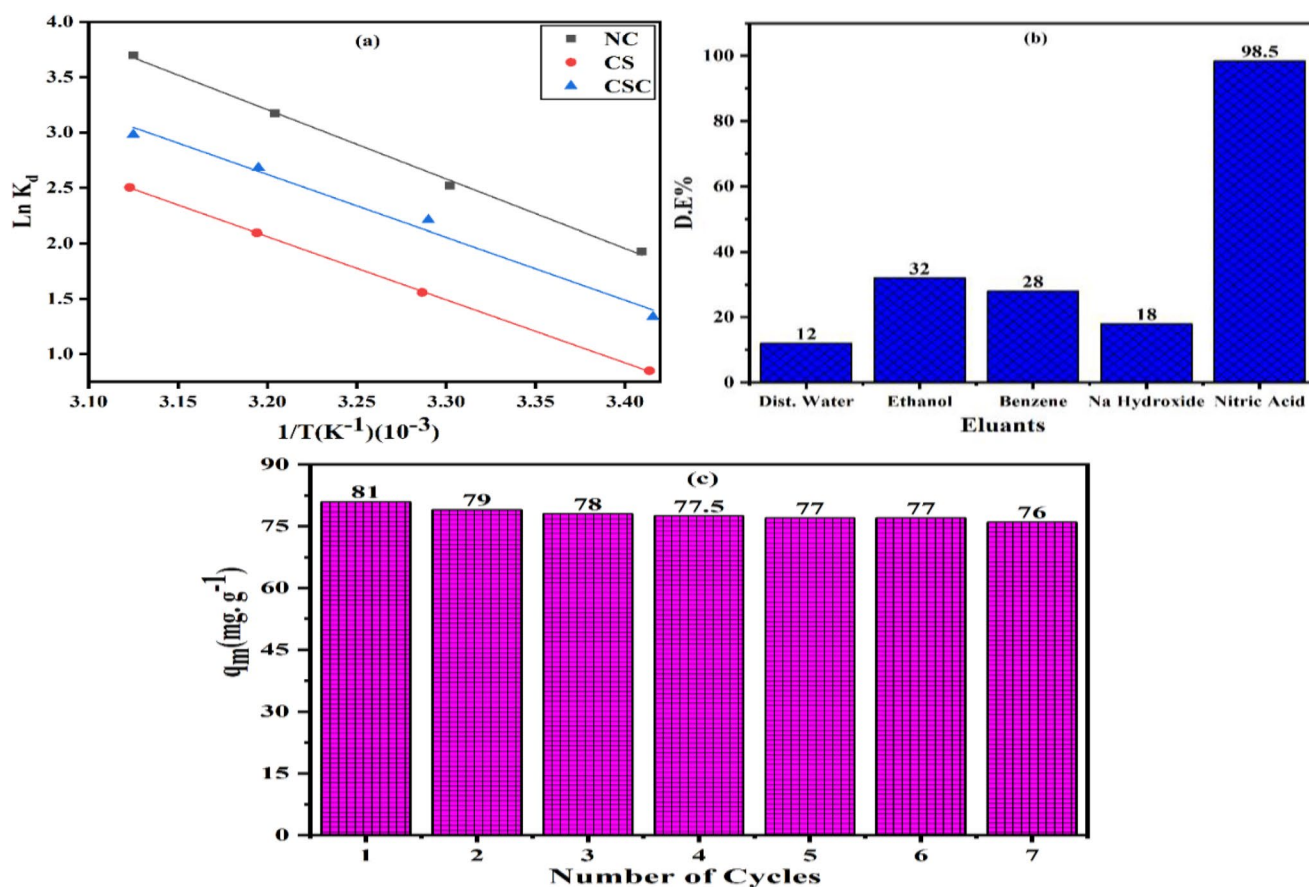


Fig. 6 Van't Hoff plot (a), MB desorption from CSC using different eluents (b), and reusability of CSC after seven adsorption and desorption cycles (c) (pH7, 2 g. L⁻¹ as adsorbent dosage, 600 mg. L⁻¹ as MB concentration, 20 °C, and 24 h as a shaking time.)

Table 4 Maximum adsorption capacity of CSC in comparison to other adsorbents

Adsorbents	q _m (mg. g ⁻¹)	References
Metakaolin-based geopolymers foam	12.5	[11]
Nanohydroxyapatite/chitosan bio composites (nHCB)	84.9	[32]
CuMn ₂ O ₄ /chitosan composites	54.0	[33]
Yucca leave derived cellulose nanofibers	82.8	[39]
Magnetized corn cob	13.2	[57]
MnO ₂ @rGO nanocomposite	156.2	[58]
Natural clay	113.6	[59]
Foamed metakaolin geopolymer	39.5	[62]
Lemon peel (LP)	79.1	[63]
CSC	301.2	Present study

3.4 Contrast between CSC and Other Published Adsorbents

The highest Langmuir capacity of adsorption of CSC as a solid adsorbent for MB adsorption in comparison with the previous solid adsorbents are listed in Table 4 [11, 32, 33, 39, 57–59, 62, 63]. The outcomes in Table 4 reveal that CSC

is a feasible adsorbent for eliminating MB from wastewater due to its larger surface area.

4 Conclusion

Utilizing natural adsorbents in contaminated water treatment systems is a promising strategy since it improves the removal of dye from wastewater. In this study, methylene blue removal from water was examined by batch adsorption procedures utilizing adsorbents such as chitosan (CS), nanocellulose/chitosan composite (CSC), and nanocellulose produced from the plant loofah sponge (NC). According to the characterization investigations, CSC exhibited adequate thermal stability, maximum specific surface area (639.3 m². g⁻¹), mesoporous radius of 2.012 nm, ultimate total pore volume (0.366 cm³. g⁻¹), and average particle size of 51.8 nm. The accurate insertion of chitosan pellets into nanocellulose by composite synthesis resulted in additional unique chemical functional groups on the CSC surface integrating the amino group and the hydroxyl groups of CS and hydroxyl groups of NC, greater activity at surface

sites, as well as more exterior pores. The experimental results of batch adsorption revealed that CSC had the maximum Langmuir adsorption capacity by using 2 g. L⁻¹ of solid dose at pH=7 and 47 °C for 24 h as shaking time, where adsorption capacity of CSC (301.20 mg. g⁻¹) > CS (261.78 mg. g⁻¹) > NC (136.80 mg. g⁻¹) by 13.1 and 54.6%, respectively, compared with CSC. Thermodynamic and kinetic tests confirmed the best fitting of Elovich, PSO, and Van't Hoff models with physisorption, spontaneous, and endothermic nature. Nitric acid achieved the highest desorption efficiency percent (98.5%). The increased reusability of CSC was examined through seven cycles of methylene blue adsorption/desorption with just 6.2% of its adsorption effectiveness decreasing. Previous results demonstrate the remarkable adsorption nature and unique features of CSC in wastewater treatment.

Supplementary Information The online version contains supplementary material available at <https://doi.org/10.1007/s10904-024-03150-z>.

Author Contributions [AFH]: Conceptualization, [EAM]: Methodology, [NME]: Formal analysis and investigation, [GE]: Writing-original draft preparation, [AFH, NME]: Writing-review and editing.

Funding Open access funding provided by The Science, Technology & Innovation Funding Authority (STDF) in cooperation with The Egyptian Knowledge Bank (EKB).

Data Availability No datasets were generated or analysed during the current study.

Declarations

Ethical Approval Not applicable.

Informed Consent Not applicable.

Consent for Publication Not applicable.

Conflict of Interest The authors declare that they have no known competing financial interests or personal relationships that could have appeared to influence the work reported in the submitted manuscript.

Competing Interests The authors declare no competing interests.

Open Access This article is licensed under a Creative Commons Attribution 4.0 International License, which permits use, sharing, adaptation, distribution and reproduction in any medium or format, as long as you give appropriate credit to the original author(s) and the source, provide a link to the Creative Commons licence, and indicate if changes were made. The images or other third party material in this article are included in the article's Creative Commons licence, unless indicated otherwise in a credit line to the material. If material is not included in the article's Creative Commons licence and your intended use is not permitted by statutory regulation or exceeds the permitted use, you will need to obtain permission directly from the copyright holder. To view a copy of this licence, visit <http://creativecommons.org/licenses/by/4.0/>.

References

1. R. Wu, A.S. Abdulhameed, S.K. Yong, Z.A. ALOthman, L.D. Wilson, A.H. Jawad, *J. Inorg. Organomet. Polym. Mater.* **34**, 1523 (2023)
2. E. Elanthamilan, I.B. Elizabeth, S.-F. Wang, I.S. Lydia, *Opt. Mater. (Amst)*. **137**, 113565 (2023)
3. H.A. Said, I. Ait Bourhim, A. Ouarga, I. Iraola-Arregui, M. Lahcini, A. Barroug, H. Noukrati, and H. Ben youcef, *Int. J. Biol. Macromol.* **225**, 1107 (2023)
4. O.H. Abuzeayad, A.M. El-Khawaga, H. Tantawy, M. Gobara, M.A. Elsayed, *J. Inorg. Organomet. Polym. Mater.* (2024)
5. K.S. Obayomi, S.Y. Lau, M.K. Danquah, J. Zhang, T. Chiong, L. Meunier, S.R. Gray, M.M. Rahman, *Desalination*. **564**, 116749 (2023)
6. M. Jamil, M.N. Akhtar, M. Imran, A. Javaid, H.K. Zafar, M. Sohail, M.A. AlDamen, M. Fitta, M.A. Khanfar, R.A. Al-Qawasmeh, *J. Photochem. Photobiol Chem.* **446**, 115095 (2024)
7. A.P. Shende, R. Chidambaram, *Heliyon*. **9**, e15228 (2023)
8. J. Wang, S. Yuan, X. Dai, B. Dong, *Chemosphere*. **319**, 138018 (2023)
9. S. Sharan, P. Khare, R. Shankar, A. Tyagi, A. Khare, *J. Taiwan. Inst. Chem. Eng.* **144**, 104739 (2023)
10. S.F. AbuQamar, H.I. Abd El-Fattah, M.M. Nader, R.A. Zaghoul, T.A. Abd El-Mageed, S. Selim, B.A. Omar, W.F. Mosa, A.M. Saad, K.A. El-Tarabily, M.T. El-Saadony, *Mar. Environ. Res.* **190**, 106068 (2023)
11. F. Eshghabadi, V. Javanbakht, *J. Mol. Struct.* **1295**, 136639 (2024)
12. A. Grich, T. Bouzid, A. Naboulsi, A. Regti, A.A. Tahiri, M.E. Himri, M. El Haddad, *J. Mol. Struct.* **1295**, (2024)
13. S.F. Sun, H.F. Wan, X. Zhao, C. Gao, L.P. Xiao, R.C. Sun, *Int. J. Biol. Macromol.* **253**, 126688 (2023)
14. A.H. Jawad, U.K. Sahu, N.A. Jani, Z.A. ALOthman, L.D. Wilson, *Surf. Interfaces*. **28**, 101698 (2022)
15. A. Reghioua, D. Barkat, A.H. Jawad, A.S. Abdulhameed, M.R. Khan, *Sustain. Chem. Pharm.* **20**, 100379 (2021)
16. C. Osagie, A. Othmani, S. Ghosh, A. Malloum, Z. Kashitarash, Esfahani, S. Ahmadi, *J. Mater. Res. Technol.* **14**, 2195 (2021)
17. F. Anoob, S. Arachchi, H.M. Azamathulla, N. Al-mahbashi, U. Rathnayake, *Case Stud. Chem. Environ. Eng.* **9**, 100639 (2024)
18. E.I. El-Aswar, H. Ramadan, H. Elkik, A.G. Taha, *J. Environ. Manage.* **301**, 113908 (2022)
19. E.Z. Gomaa, *J. Inorg. Organomet. Polym. Mater.* **32**, 4114 (2022)
20. A.F. Hassan, G.A. El-Naggar, G. Esmail, W.A. Shaltout, *Appl. Surf. Sci. Adv.* **13**, 100388 (2023)
21. B. Aoudi, Y. Boluk, M. Gamal El-Din, *Sci. Total Environ.* **843**, 156903 (2022)
22. C.R. Bauli, G.F. Lima, A.G. de Souza, R.R. Ferreira, D.S. Rosa, *Colloids Surf. Physicochem Eng. Asp.* **623**, 126771 (2021)
23. A. Shahzad, M.W. Ullah, J. Ali, K. Aziz, M.A. Javed, Z. Shi, S. Manan, M. Ul-Islam, M. Nazar, G. Yang, *Sci. Total Environ.* **858**, 159937 (2023)
24. S. Hong, Y. Song, Y. Yuan, H. Lian, H. Liimatainen, *Ind. Crops Prod.* **143**, 111913 (2020)
25. A.A. Oun, K.H. Kamal, K. Farroh, E.F. Ali, M.A. Hassan, *Arab. J. Chem.* **14**, 103281 (2021)
26. M.T. Hasanin, S.A. Elfeky, M.B. Mohamed, R.M. Amin, *J. Inorg. Organomet. Polym. Mater.* **28**, 1502 (2018)
27. V. Pawariya, S. De, J. Dutta, *Carbohydr. Polym.* **323**, 121395 (2024)
28. A.H. Jawad, S. Rangabhashiyam, A.S. Abdulhameed, S.S.A. Syed-Hassan, Z.A. ALOthman, L.D. Wilson, *J. Polym. Environ.* **30**, 2759 (2022)

29. D.H. Micheletti, J.G. da Silva Andrade, C.E. Porto, B.H.M. Alves, F.R. de Carvalho, O.A. Sakai, V.R. Batistela, *Bioresour Technol. Rep.* **24**, (2023)
30. S. Radoor, J. Karayil, A. Jayakumar, D.R. Kandel, J.T. Kim, S. Siengchin, J. Lee, *Carbohydr. Polym.* **323**, 121339 (2024)
31. N.C. Das, M.M. Rahman, S.F. Kabir, *Int. J. Biol. Macromol.* **249**, 126136 (2023)
32. T.S. Trung, N.C. Minh, H.N. Cuong, P.T.D. Phuong, P.A. Dat, P.V. Nam, N. Van Hoa, *J. Sci. Adv. Mater. Devices.* **7**, 100485 (2022)
33. M. Samadi Kazemi, A. Sobhani, *Arab. J. Chem.* **16**, 104754 (2023)
34. W.A. Shaltout, G.A. El-Naggar, G. Esmail, A.F. Hassan, *Biomass Convers. Biorefinery* (2022)
35. A.F. Hassan, R. Hrdina, *Int. J. Biol. Macromol.* **109**, 507 (2018)
36. L.M. Alshandoudi, S.R. Alkindi, T.Y. Alhatmi, A.F. Hassan, *Biomass Convers. Biorefinery* (2023)
37. B. Jia, F. Feng, X. Wang, Y. Song, F. Zhang, *J. Futur Foods.* **4**, 1 (2024)
38. A. Reghioua, D. Barkat, A.H. Jawad, A.S. Abdulhameed, S. Rangabhashiyam, M.R. Khan, Z.A. ALothman, *J. Polym. Environ.* **29**, 3932 (2021)
39. A. Naderahmadian, B. Eftekhari-Sis, H. Jafari, M. Zirak, M. Padervand, G. Mahmoudi, M. Samadi, *Int. J. Biol. Macromol.* **247**, 125753 (2023)
40. Z. Peng, S. Wang, Y. Wu, X. Liu, H. Liu, D. Zhang, L. Fu, *Micro-porous Mesoporous Mater.* **363**, 112826 (2024)
41. A.F. Hassan, A.A. Mustafa, G. Esmail, A.M. Awad, *Arab. J. Sci. Eng.* **48**, 353 (2023)
42. M. Sahli, S. Rudz, K. Chetehouna, R. Bensaha, M. Korichi, *Mater. Chem. Phys.* **301**, 127635 (2023)
43. W. Zhu, M. Chen, J. Jang, M. Han, Y. Moon, J. Kim, J. You, S. Li, T. Park, J. Kim, *Carbohydr. Polym.* **323**, 121393 (2024)
44. Y.A. Hamdan, S. Elouali, N. Eladlani, B. Lefevre, H. Oudadesse, M. Rhazi, *Int. J. Biol. Macromol.* **252**, 126292 (2023)
45. V. Chaparala, G. Ravi Kiran, Sastry, P. Phani, Prasanthi, *Mater. Today Proc.* (2023)
46. S. Das, A.K. Chaudhari, V.K. Singh, A.K. Dwivedy, N.K. Dubey, *Food Chem.* **430**, 137038 (2024)
47. Z.M. Zain, A.S. Abdulhameed, A.H. Jawad, Z.A. ALothman, Z.M. Yaseen, *J. Polym. Environ.* **31**, 501 (2023)
48. Y.O. Al-Ghamdi, *Arab. J. Chem.* **15**, 104066 (2022)
49. M.H. Salim, Z. Kassab, Y. Abdellaoui, A. García - Cruz, A. Soumare, E. Ablouh, and M. El Achaby, *Int. J. Biol. Macromol.* **210**, 639 (2022)
50. S. Moalla, I. Ammar, M.L. Fauconnier, S. Danthine, C. Blecker, S. Besbes, H. Attia, *Int. J. Biol. Macromol.* **183**, 254 (2021)
51. D. Bajer, *Int. J. Biol. Macromol.* **249**, 126103 (2023)
52. X. Xu, X. Ouyang, L.Y. Yang, *J. Mol. Liq.* **322**, 114523 (2021)
53. R. Ebrahimi, M. Fathi, H.B. Ghodduzi, *Int. J. Biol. Macromol.* **242**, 124704 (2023)
54. E. Moradi, M. Fathi, *Bioact Carbohydrates Diet. Fibre.* **30**, 100378 (2023)
55. N. Sboui, F. Dhaouadi, M. Jabli, A. Ben, Lamine, K. Boughzala, *Inorg. Chem. Commun.* **157**, 111386 (2023)
56. L.L. Zhang, A. Zaoui, W. Sekkal, *J. Water Process. Eng.* **57**, 104651 (2024)
57. N.B. Allou, M.A. Tigori, A.A. Koffi, M. Halidou, N.S. Eroï, P. Atheba, A. Trokourey, *Sci. Afr.* **21**, 1 (2023)
58. T.S. Munonde, A. Nqombolo, S. Hobongwana, A. Mpupa, P.N. Nomngongo, *Heliyon.* **9**, e15502 (2023)
59. Z. Bingül, *J. Mol. Struct.* **1250**, (2022)
60. A.F. Hassan, G.A. El-Naggar, A.G. Braish, M.M.A. El-Latif, W.A. Shaltout, M.S. Elsayed, *J. Inorg. Organomet. Polym. Mater.* (2023)
61. C.S.T. Araújo, I.L.S. Almeida, H.C. Rezende, S.M.L.O. Marcionilio, J.J.L. Léon, T.N. de Matos, *Microchem J.* **137**, 348 (2018)
62. S. Candamano, G. Coppola, A. Mazza, J.I. Caicho Caranqui, S. Bhattacharyya, S. Chakraborty, F. Alexis, C. Algieri, *Chem. Eng. Res. Des.* **197**, 761 (2023)
63. İ. Küçük, *Chem. Data Collect.* **46**, 1 (2023)

Publisher's Note Springer Nature remains neutral with regard to jurisdictional claims in published maps and institutional affiliations.